Nanoscale

PAPER

View Article Online
View Journal | View Issue

Cite this: *Nanoscale*, 2026, **18**, 8707

Design and fabrication of plasmonic hedgehog-shaped covalent organic framework nanocomposites for indirect SERS-based ultradetection of water contaminant terbutryn

Tolga Zorlu, [a,b] Maedeh Anisi,[b] Monica Quarato,[c] Ana Vieira,[c] Jesús Giráldez-Martínez, [b] Carlos Gonçalves,[c] Aitor Alvarez,[c] Tania Prieto,[b] Dana D. Medina,[d] Lucas V. Besteiro, *[b] Miguel A. Correa-Duarte,[b] Begoña Espiña, [c] Laura M. Salonen *[b,c] and Laura Rodriguez-Lorenzo *[c]

Surface-enhanced Raman scattering (SERS) spectroscopy is an ultrasensitive analytical technique, the efficiency of which can be enhanced by developing plasmonic nanostructured substrates and sieving elements to capture target analytes near the plasmonic surface. This study reports the development of a plasmonic hedgehog-shaped colloidal covalent organic framework (SiO_2@Au@ $COF_{Hedgehog}$) composite as an efficient SERS substrate. First, hedgehog-shaped COF particles were synthesized, fully characterized, and their development was studied over time to gain insight into their formation. Then, SiO_2@Au@$COF_{Hedgehog}$ composite was prepared, retaining the characteristics of the crystalline COF and the hedgehog-type morphology. The composite exhibited significantly enhanced SERS intensity for 4-nitrothiophenol (4-NTP), which has a strong affinity for the Au surface *via* S–Au bond formation, achieving a limit of detection (LoD) of 10^{-10} M. This demonstrated that molecules with high affinity for the Au surface and smaller than the COF pore size (<3 nm) can diffuse easily through the pore. Furthermore, an indirect SERS strategy for the detection of the toxic herbicide terbutryn was designed based on the reduction of the nitro group in 4-NTP to form 4,4-dimercaptoazobenzene (DMAB). This process is attributed to the proximity of terbutryn to the 4-NTP-coated AuNPs, facilitated by the high adsorption efficiency of the porous anisotropic COF shell for this herbicide (>50%). A strong correlation was found between the SERS intensity ratios of specific peaks, achieving an impressive LoD of 10^{-9} M (220 ng L^{-1}). Overall, these findings underscore the potential of plasmonic hedgehog-shaped COF composites as innovative nanomaterials for SERS-based detection, highlighting the exciting possibilities for developing sensitive and selective sensors for various target molecules, with implications in environmental analysis, biomedicine, and fields requiring ultrasensitive analytical techniques.

Received 10th June 2025,
Accepted 4th March 2026

DOI: 10.1039/d5nr02476e

rsc.li/nanoscale

Introduction

Nearly 80% of the world's population is currently at risk of water insecurity and has limited access to clean water.[1] Some of the most toxic water pollutants for humans and species living in aquatic ecosystems are organic compounds used as pharmaceuticals, pesticides, or personal care products.[2,3] Hence, it is necessary to understand their environmental occurrence and concentration, usually in the ppb–ppt range, with enough spatial and temporal resolution to make efficient management and regulation decisions. Therefore, the development of innovative technological and scientific approaches for pollutant monitoring is essential. However, detecting these compounds in natural waters is challenging due to the sensitivity requirements, usually needing extensive pre-treatment and expensive equipment. Therefore, there is an urgent need for efficient approaches capable of detecting pollutant molecules at very low concentrations.

Surface-enhanced Raman scattering (SERS) spectroscopy is a highly efficient, ultrasensitive analytical technique applicable across diverse fields.[4] The underlying principle of this tech-

[a]*Department of Physical and Inorganic Chemistry, Universitat Rovira i Virgili, Carrer de Marcel·lí Domingo s/n, 43007 Tarragona, Spain*
[b]*CINBIO, University of Vigo, 36310 Vigo, Spain. E-mail: lucas.v.besteiro@uvigo.es, lauramaria.salonen@uvigo.es*
[c]*International Iberian Nanotechnology Laboratory (INL), Avenida Mestre José Veiga, 4715-330 Braga, Portugal. E-mail: laura.rodriguez-lorenzo@inl.int*
[d]*Department of Chemistry and Center for Nanoscience (CeNS), Ludwig-Maximilians-University, Butenandtstraße 11 (E), 81377 Munich, Germany*

nique is the immense amplification of Raman signals from analytes of interest through the utilization of nanoparticles (NPs) with plasmonic properties, such as Au, Ag, or Cu. In recent years, substantial efforts have been directed towards the enhancement of the plasmonic characteristics of these nanoparticulate substrates, which significantly influence the efficacy of SERS spectroscopy,[5–7] *e.g.*, by individual isolation of anisotropic plasmonic NPs, such as nanostars and nanorods, which are prone to aggregation in the analytical medium,[8,9] synergistic combination of different plasmonic materials,[10] and the fabrication of novel generations of composite materials that integrate various sieving elements for the selective SERS-based detection of target molecules.[11–14]

The introduction of sieving elements to SERS substrates is essential to allow for the SERS-based detection of analytes that do not feature functionalities with affinity to the surface of the plasmonic materials.[15] Novel porous materials, such as metal–organic frameworks (MOFs) and covalent organic frameworks (COFs), are attractive sieving elements, either in isolation or in conjunction with plasmonic NPs,[16–19] due to their defined and uniform pore sizes, tuneable pore surface functionalities, and high adsorption capacities.[20–22] In previous years, numerous studies have demonstrated that MOFs can be integrated with plasmonic NPs and used for SERS-based detection of various molecules. For instance, Au NPs encapsulated within MOFs, coupled onto a gold film, facilitated the detection of multiple volatile organic compounds using SERS spectroscopy.[23] In another study, plasmonic MOF structures enriched with magnetic NPs were utilized to detect organophosphorus pesticides.[24] On the other hand, COFs can offer advantages over MOFs, including their light weight, high stability in water, and large pore sizes.[25] However, the utilization of COFs in SERS-based applications is currently in early stages of development. First examples have recently emerged using COF composites with Ag,[26] Au,[27] and both Au and Pd NPs.[28]

One of the main reasons for the scarcity of the reported studies using COFs is undoubtedly related with the challenges to obtain crystalline COF–plasmonic nanoparticle composites with defined sizes. In addition, the colloidal stability issues observed in several COF-based SERS substrates can lead to aggregation of the plasmonic COF structures, directly causing a decrease in the effective performance of the SERS substrate.

To date, few examples exist of colloidally stable COF structures,[29] typically involving the use of nitrile-based solvents in the synthesis.[30–32] On the other hand, hedgehog-shaped particles, spheres densely decorated with rigid nanoscale spikes, have emerged as popular materials due to their remarkable colloidal stability.[33,34] Such nanoparticles are typically produced through two-step reactions, involving the synthesis of an organic or inorganic core material followed by the localization of "spike" materials on the surface of the core. These geometries formed solely from organic building blocks are relatively rare. Within the realm of COFs, the materials most closely resembling this morphology are three-dimensional urchin-shaped particles,[35,36] with the syntheses relying *e.g.*, on the use of nitrile-based solvents[37] or two-step incubation procedures.[38] To date, few examples of this type of COF particles have been reported, with most materials featuring 1,3,5-tris(4-aminophenyl)benzene (TAPB) as a building block. However, with relatively short and randomly arranged spikes, these COFs with spike-like morphologies have limited long-term dispersion capabilities in solution.

Herein, we report the synthesis of imine-linked hedgehog-shaped COF particles, $COF_{Hedgehog}$, using a simple one-step process at room temperature, without the need of core template materials or additional incubation steps. Extensive characterization gave insight into the formation of the particles and the influence of different synthesis conditions on the morphology. Subsequently, the developed procedure was adapted to gain access to plasmonic SiO_2@Au@$COF_{Hedgehog}$ composites. Remarkably, the composite served as a highly effective SERS substrate owing to the dispersibility and sieving ability of the $COF_{Hedgehog}$ material, allowing for the proximity of the analytes to the plasmonic NP surface, paving the way to selective ultradetection of contaminants in complex matrices.

Results and discussion

To gain access to COF nanoparticles, 2,5-dimethoxyterephthaldehyde (DMTP) and TAPB monomers, in a molar ratio of TAPB/DMTP 0.67 : 1, were reacted at room temperature for 72 h in acetonitrile with aqueous 12 M acetic acid (AcOH) as the catalyst (Fig. 1a). The reaction yielded $COF_{Hedgehog}$ particles characterized by notably long spikes (103 ± 12 nm) and particle sizes of 526 ± 29 nm (Fig. 1b, c and S1), as confirmed by transmission electron microscopy (TEM) and scanning electron microscopy (SEM). The reproducibility of the $COF_{Hedgehog}$ synthesis was evaluated by preparing three independent batches following the procedure described in the SI. PXRD analysis of the main reflection ($2\theta \approx 2.79°$) showed minimal batch-to-batch variation, with an inter-batch RSD of 7.7%, confirming consistent crystallinity. Particle sizes from FESEM images were also measured, with intra-batch RSDs ranging from 5.45% to 7.19%, indicating consistent particle morphology across independent syntheses (see Tables S1, S2, and Fig. S1c–f in the SI for details).

The powder X-ray diffraction (PXRD) pattern of the $COF_{Hedgehog}$ particle sample was indexed according to previous reports regarding its eclipsed AA stacking model.[39–42] Hereby, the distinct reflection at 2.79° corresponds to the (100) plane, and the additional reflections at 4.84°, 5.65°, 7.39°, and 9.76° correspond to the (110), (200), (210), and (220) planes, respectively (Fig. 1d and S2). N_2 physisorption at 77 K revealed a type IV isotherm typical of mesoporous materials (Fig. 1e), with a Brunauer–Emmett–Teller (BET) surface area (S_{BET}) calculated to be *ca.* 550 $m^2\ g^{-1}$. Barrett–Joyner–Halenda (BJH) pore size analysis indicated the particles primarily exhibit a pore size of 3.2 nm within a narrow distribution range, along with moderate contributions from 3.0 nm pores and minor contributions from pores with sizes of 1.4 and 1.7 nm (Fig. S3). Additionally, the particles demonstrated excellent stability in water, retain-

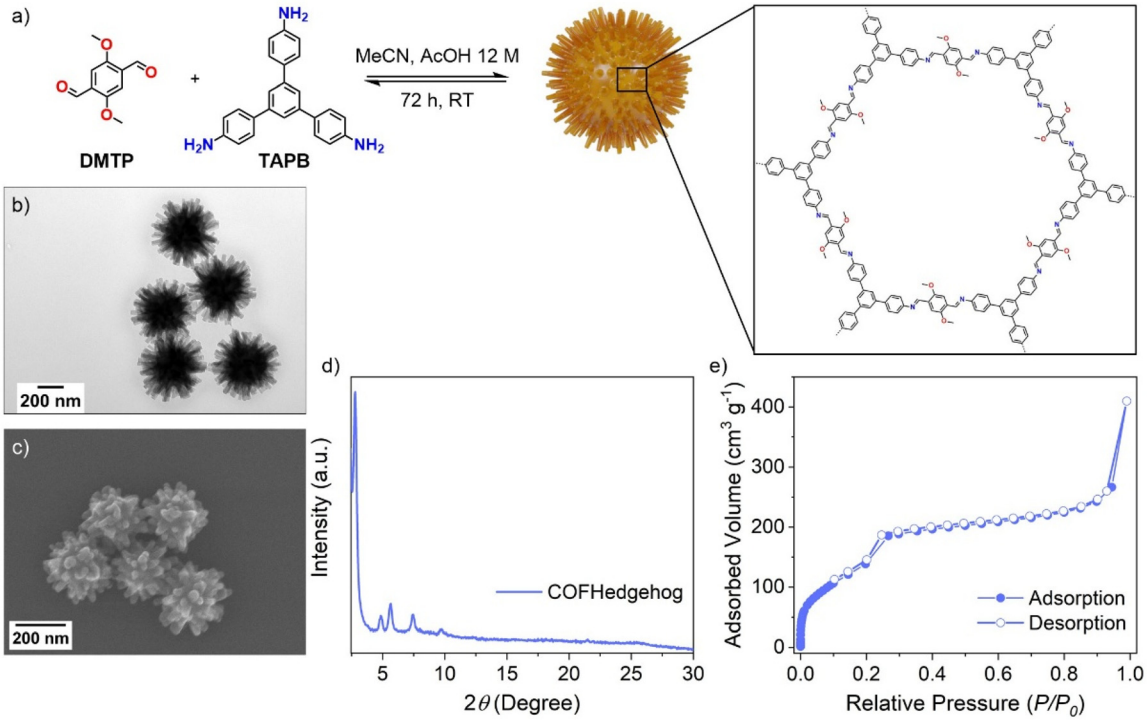

Fig. 1 (a) Synthesis scheme and illustration of $COF_{Hedgehog}$ particles. Color code: red = O, cyan = N, and grey = C. (b and c) TEM and SEM images of $COF_{Hedgehog}$ particles, respectively. (d) PXRD pattern and (e) N_2 physisorption isotherm of $COF_{Hedgehog}$ particles.

ing their crystalline structure even after two weeks of immersion (Fig. S4).

UV-Vis spectroscopy revealed that $COF_{Hedgehog}$ particles efficiently absorb light in the visible range, with a primary absorbance band centered at 491 nm in acetonitrile (Fig. S5). Raman spectroscopy was employed to analyze the vibrational spectra of both monomers and $COF_{Hedgehog}$ particles in the solid state (Fig. S6). Using an excitation wavelength of 785 nm, the spectrum of $COF_{Hedgehog}$ showed the disappearance of the bands at 1681 and 1354 cm^{-1} attributed to C=O of DMTP and NH_2 of TAPB, respectively, as well as the emergence of a new band at 1586 cm^{-1}, corresponding to the C=N vibration mode, confirming the successful formation of the imine linkages.[43]

For comparison, bulk TAPB-DMTP COF (COF_{Bulk}) was also synthesized under the same conditions as $COF_{Hedgehog}$ but at an elevated temperature of 120 °C. Raman spectroscopy confirmed that both COF_{Bulk} and $COF_{Hedgehog}$ exhibited identical characteristic peaks (Fig. S7). However, TEM imaging revealed that COF_{Bulk} was randomly oriented intergrown material, albeit also displaying a hedgehog-like morphology (Fig. 2a), whereas room-temperature synthesis resulted in $COF_{Hedgehog}$ particles (Fig. 2b). The PXRD patterns indicated that both materials possessed long-range order (Fig. S7b). Notably, only the $COF_{Hedgehog}$ particles maintained dispersibility in water over time (Fig. 2c and d). The zeta potential of $COF_{Hedgehog}$ particles was also significantly higher (+28 ± 2 mV) as compared to that of COF_{Bulk} (+14 ± 1 mV) (Fig. S7c), which likely stems from positively charged surface groups due to protonation,[44] contributing to the enhanced colloidal stability of $COF_{Hedgehog}$. In addition, the unique hedgehog morphology has been shown to promote long-term colloidal dispersibility by preventing particle aggregation.[33]

Next, we aimed to understand the relationship between COF particle morphology and reaction conditions. We initially investigated the effect of the monomer molar ratio by synthesizing COFs at room temperature for 72 h with [TAPB]/[DMTP] ratios ranging from 0.34 : 1 to 1.33 : 1 to confirm if deviations from the ideal 0.67 : 1 stoichiometric ratio influence the particle morphology. TEM images confirmed that the resulting particles exhibited notably diverse morphologies (Fig. S8). At a molar ratio of 0.34 : 1, small, non-ordered amorphous spherical particles with three-dimensional structures were formed. In contrast, increasing the TAPB ratio above 0.67 led to the formation of highly crystalline COFs, as confirmed by PXRD analysis, but TEM images indicated irregular particle morphologies (Fig. S8c and d). These materials quickly lost their colloidal stability, becoming poorly dispersed in water. On the other hand, particles synthesized with lower TAPB content displayed prolonged stability in water due to their well-defined morphology, maintaining a stable dispersion over time.

We then examined the impact of the concentration of AcOH catalyst on both morphology and crystallinity while keeping the monomer ratio constant at [TAPB]/[DMTP] 0.67 : 1. Reactions were conducted at room temperature for 72 h using AcOH catalyst concentrations of 3, 6, 12, and 16 M. Although

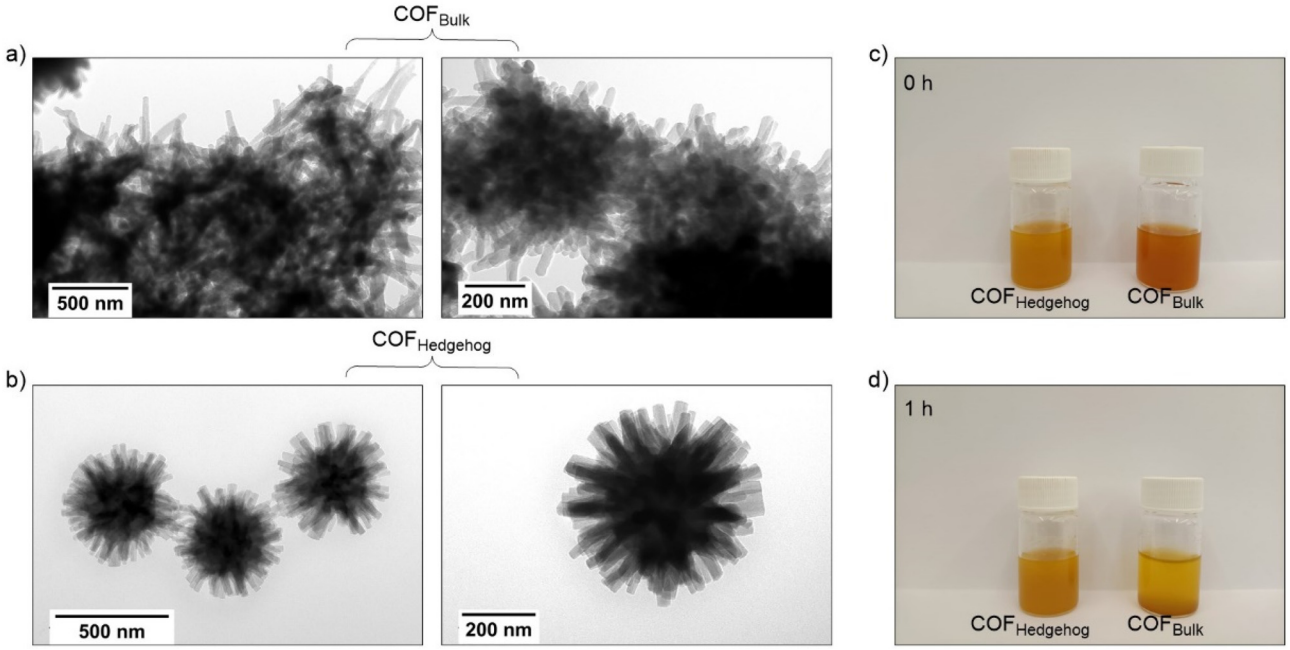

Fig. 2 Comparison of COF_{Bulk} and $COF_{Hedgehog}$. (a and b) TEM images of COF_{Bulk} and $COF_{Hedgehog}$ particles under higher and lower magnifications. (c and d) Colloidal stabilities of COF_{Bulk} and $COF_{Hedgehog}$ particle solutions at t = 0 h and 1 h, respectively.

particles were formed under all conditions (Fig. S9), only the AcOH concentration of 12 M afforded well-defined crystalline $COF_{Hedgehog}$ particles. Lower AcOH concentrations resulted in polydisperse particles, while higher AcOH concentrations produced monodisperse particles with rough, spherical surfaces. Insufficient AcOH catalyst reduces the reversibility of the COF-forming condensation reaction, limiting error-correction and thus leading to polydisperse particles.[45,46] At high AcOH concentration, the increased catalytic activity[47] enhances bond reversibility and promotes rapid nucleation and growth pathways,[48] resulting in more monodisperse particles. However, excess AcOH may also induce very rapid nucleation and precipitation, leading to the formation of nanoparticle aggregates followed by structural reorganization during crystallization,[49] which can give rise to rough, spherical morphologies in polycrystalline COFs.

To gain deeper insight into the influence of the solvent on COF particle morphology, a 2 : 1 acetonitrile/benzonitrile mixture—more viscous than pure acetonitrile—was employed as the reaction solvent for polycrystalline COF synthesis. All other parameters were kept identical to those used in the preparation of $COF_{Hedgehog}$ particles (Fig. S10). PXRD analysis confirmed the formation of highly crystalline COFs; however, SEM images revealed spherical particle morphologies lacking spiky features (Fig. S10b and d). We attribute this to the higher viscosity of benzonitrile relative to acetonitrile, which can enhance colloidal stability during COF particle formation, thereby promoting isotropic growth of the particles. This morphological outcome suggests that the synthesis process is primarily governed by kinetic factors.[50] We also carried out the synthesis at 80 °C using the same [TAPB]/[DMTP] ratio, solvent system, and AcOH concentration as in the $COF_{Hedgehog}$ synthesis. Under these conditions, PXRD patterns confirmed the formation of crystalline COFs, while SEM images showed spherical morphologies, similar to those observed in the solvent viscosity variation experiment (Fig. S10c and d). This finding reflects the fact that reaction temperature can alter the morphology of the COFs,[51] likely by affecting the balance between nucleation and growth rates. The formation of spiky $COF_{Hedgehog}$ particles under low-viscosity, low-temperature conditions, and the transition to spherical morphologies with either increased solvent viscosity or reaction temperature, strongly indicate that particle shape is governed by kinetic factors. These findings indicate that the key factors governing the formation of $COF_{Hedgehog}$ particles are (i) temperature, (ii) the molar ratio of reacting monomers, (iii) solvent, and (iv) catalyst concentration, with $COF_{Hedgehog}$ particles forming exclusively under room temperature conditions in acetonitrile at the [TAPB]/[DMTP] ratio of 0.67 : 1 and [AcOH] = 12 M.

To further investigate the time-dependent formation of hedgehog-shaped COF particles, we sampled the reaction at time intervals of 1, 12, 24, 48, and 72 h (Fig. 3). TEM images (Fig. 3b–f) revealed that after 1 h, the particles exhibited a uniform spherical morphology. However, even at this stage, the surface was not perfectly smooth, as small protrusions (~20 ± 5 nm) had already begun to form. As the reaction progressed, the particles color-shifted from yellow to orange, and the final particle size and tip length increased to 527 ± 29 nm and 103 ± 12 nm, respectively (Fig. 3g, h and S11). Interestingly, the core size decreased from 300 ± 17 nm at 1 h to 220 ± 19 nm at 72 h (Fig. 3i and S11). This could indicate that, in addition to the monomers in the reaction medium

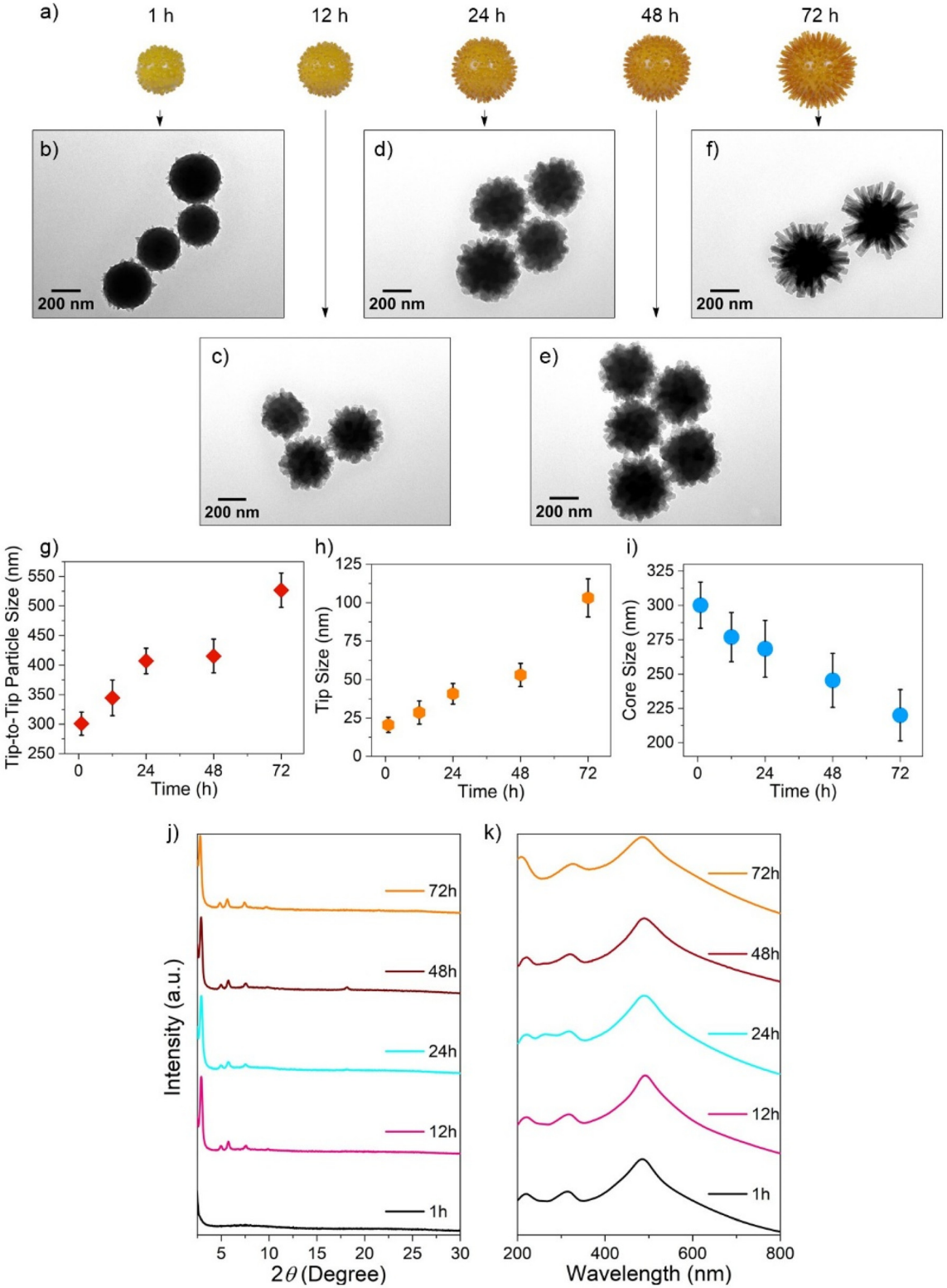

Fig. 3 (a) Schematic illustration of morphological evolution of $COF_{Hedgehog}$ particles over time. (b–f) TEM images of the particles taken at different time intervals. (g–i) Changing of the total, tip, and core size of the particles over time, respectively. The error bars indicate the mean ± standard error of number of particles (N = 100). (j) PXRD patterns and (k) UV-vis spectra of $COF_{Hedgehog}$ particles at different time intervals. (l) Changing λ_{max} of $COF_{Hedgehog}$ particles at different time intervals: 484 nm (1 h), 485 nm (12 h), 489 nm (24 h), 489 nm (48 h), and 491 nm (72 h).

that contribute to the growth of the particle size through a self-assembly phenomenon,[52] etching of the amorphous core formed within the first hour (Fig. 3j, 1 h) contributes to the growth of the tips facilitated by the reversible nature of the imine linkages at room temperature. As a result, the tips could form *via* a self-correction mechanism typical of imine COFs.[37,53] However, more detailed experimental studies are required to gain mechanistic insight into the tip formation. Ordered crystalline structures begin to appear after 12 h and become increasingly pronounced as time progresses (Fig. 3j, from 12 to 72 h). Similar observations have been made when using a competing modulator compound in COF synthesis.[54]

As the tips elongate and the core shrinks, the particle-containing solutions gradually darken from yellow to deep orange. Correspondingly, the UV-Vis spectra of the particles exhibit a red shift in the intense absorption maximum (λ_{max}) from 484 nm at the end of the first hour to 491 nm after 72 h (Fig. 3k). In addition to the contributions from the monomers in the UV region, the absorbance of $COF_{Hedgehog}$ particles is influenced by the scattering properties of the large, spiked spheres. This is supported by numerical simulations conducted on purely dielectric structures with real permittivity, mimicking the geometry of the $COF_{Hedgehog}$ system. The simulated scattering spectrum (Fig. S12) qualitatively reproduces the key features observed in the experimental absorbance spectrum.

With the procedure to gain access to crystalline, monodisperse, and colloidal $COF_{Hedgehog}$ particles in hand, we fabricated SERS substrates with plasmonic NPs. Leveraging on the anisotropic morphology and colloidal stability of the $COF_{Hedgehog}$ shell, plasmonic composites with such spiky structures could enhance substrate–analyte interactions. To this end, we first prepared template-based plasmonic beads as core materials (Fig. 4a). This design of plasmonic structures has proved highly effective in numerous SERS-based detection studies, as it involves a large number of plasmonic NPs on the surface of a template material, thus enhancing the presence of hotspots resulting from the proximity of the NPs to each other.[55,56] Silica (SiO_2) beads with an approximate diameter of 488 ± 11 nm were selected as the template material (Fig. 4b and S13). The use of SiO_2 is advantageous due to its chemical inertness, allowing it to withstand high concentrations of acid during COF growth. Then, the surface of the SiO_2 beads was functionalized with a positively charged polyelectrolyte, poly (allylamine hydrochloride) (PAH), and subsequently, negatively charged spherical Au NPs with a diameter of 14.5 ± 1.7 nm were electrostatically retained on the template surface to produce the SiO_2@Au plasmonic beads (Fig. 4c and S14).

To synthesize the SiO_2@Au@$COF_{Hedgehog}$ composite, the surface of the plasmonic beads was first functionalized with 4-aminothiophenol (4-ATP) by subjecting an aqueous SiO_2@Au bead solution (0.1 mg mL^{-1}; 10 mL) to an ethanolic solution of 4-ATP (0.1 mM) overnight. The functionalization was envisioned to link the –SH moieties with the plasmonic surface while leaving the amino groups available for subsequent condensation reactions with the aldehyde functionalities of DMTP. This incorporation of anchoring groups is typically required for achieving crystalline COF composites.[57,58] Although alternative strategies that bypass this pre-functionalization step have been reported, relying on the use of excess of one of the COF building blocks,[59] finding suitable reaction conditions for such a one-step approach is not trivial and rigorous optimization of synthesis conditions may be required. Following pre-functionalization, the COF shell was grown under the conditions optimized for $COF_{Hedgehog}$ particles, resulting in hedgehog-shaped plasmonic composites (Fig. 4d). TEM images revealed that the resulting composites had a tip-to-tip size of approximately 719 ± 68 nm, with shell thicknesses of 88 ± 12 nm (Fig. S15a–c). The PXRD pattern confirmed the crystalline nature of the hedgehog-shaped COF shell, displaying reflections at 2.79°, 4.84°, 5.65°, 7.39°, and 9.76°, similar to those observed in $COF_{Hedgehog}$ particles

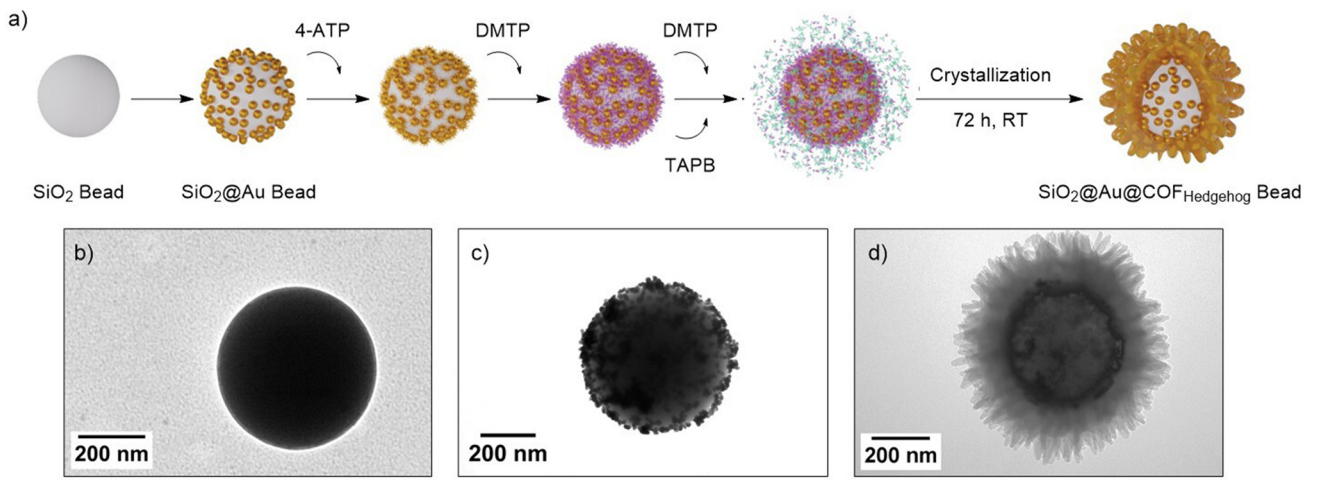

Fig. 4 (a) Schematic illustration of the preparation of SiO_2@Au@$COF_{Hedgehog}$ composites. (b–d) TEM images of SiO_2 bead, SiO_2@Au beads, and SiO_2@Au@$COF_{Hedgehog}$ composites, respectively.

(Fig. S15d). Additionally, a weak reflection near 38° was attributed to the Au NPs on the surface of the SiO_2 beads, although the signal intensity was low, likely due to the thick COF shell surrounding the SiO_2@Au@$COF_{Hedgehog}$ composites. Notably, when the bead surface was not pre-functionalized with 4-ATP, the surface remained largely bare, with only isolated "islands" of $COF_{Hedgehog}$ particles observed near the bead surface (Fig. S16), highlighting the critical role of surface pre-functionalization in promoting COF attachment. Furthermore, comparing the Raman spectra of SiO_2@Au@$COF_{Hedgehog}$ composites with those of $COF_{Hedgehog}$ particles confirmed the successful preparation of the plasmonic COF composites (Fig. S17).

Next, we evaluated the applicability of SiO_2@Au@$COF_{Hedgehog}$ as a SERS substrate. 4-Nitrothiophenol (4-NTP) was chosen as probe molecule due to its high affinity to the plasmonic surface *via* the thiol moiety. This compound has been used as a reporter for various SERS-based applications.[60,61] In addition, the SERS fingerprint of 4-NTP, specifically the peak assigned to the nitro group centred at 1330 cm^{-1}, does not overlap with the signals from the COF shell or 4-ATP (see Fig. S17). For the SERS experiment, equal amounts of substrates with and without COF shell, SiO_2@Au@$COF_{Hedgehog}$ and SiO_2@Au, were subjected to solutions of 4-NTP in ethanol at various concentrations from 10^{-5} to 10^{-11} M. After 1 h, the solutions were centrifuged to remove excess 4-NTP, the collected material was dispersed in water, and the SERS performance of the substrates was examined in liquid. The SERS measurements were conducted using a 785 nm laser and a macro setup configuration. In this setup, the laser was focused on a volume rather than a traditional area, and the scattered light was collected. The approach allows the acquisition of quantitatively reliable SERS spectra, resulting from the averaged contribution of many beads within the illuminated volume.[55] The results indicated that SiO_2@Au@$COF_{Hedgehog}$ exhibited significantly higher SERS intensity for 4-NTP as compared to SiO_2@Au without a COF shell, enhancing the sensitivity (Limit of detection (LoD) = 10^{-10} M) (Fig. 5a–b). The absolute intensity of the narrow band at 1330 cm^{-1} (nitro stretching)[62] is plotted in Fig. 5c as a function of 4-NTP concentration, demonstrating that the SERS intensity of 4-NTP in SiO_2@Au@$COF_{Hedgehog}$ was five-fold higher at 10^{-10} M than the SERS intensity in SiO_2@Au without a COF shell, 1.6-fold higher at 10^{-9} M, and 1.3–1.2-fold higher at 10^{-8}–10^{-7} M. This difference is attributed to the confinement effect generated by the COF shell as a porous material.[63,64] As 4-NTP molecules diffuse through the COF pores, this increases the localization and concentration of the molecules in a specific area of the Au surface (free area where COF is not attached). This also restricts the molecules' movement through the whole plasmonic surface, creating areas with high 4-NTP density on the Au surface. This confinement effect is stronger at higher concentrations due to several high-density self-assembled 4-NTP monolayers being formed in SiO_2@Au@$COF_{Hedgehog}$, while this pre-concentration effect is not provided in SiO_2@Au. For SiO_2@Au@$COF_{Hedgehog}$, in addition to the COF C=N stretching at 1564 cm^{-1} and the 4-NTP signals, there were also signals visible from 4-ATP (C–S stretching at 1075 cm^{-1}),[65] which acted as the functionalizing agent of the plasmonic surface, but these signals do not overlap with those of 4-NTP (Fig. S17).

Furthermore, while the Raman and SERS spectra of the COF essentially exhibited the same peaks, the dominant C=N peak observed at 1586 cm^{-1} for dry COF particles undergoes a red-shift to 1564 cm^{-1} in SiO_2@Au@$COF_{Hedgehog}$. With the SiO_2@Au substrate without a COF shell, only the SERS peaks from 4-NTP were clearly observed (Fig. S17). On the other hand, 4-NTP molecules quickly provided results after 1 h following interaction with the SiO_2@Au@$COF_{Hedgehog}$ substrates.

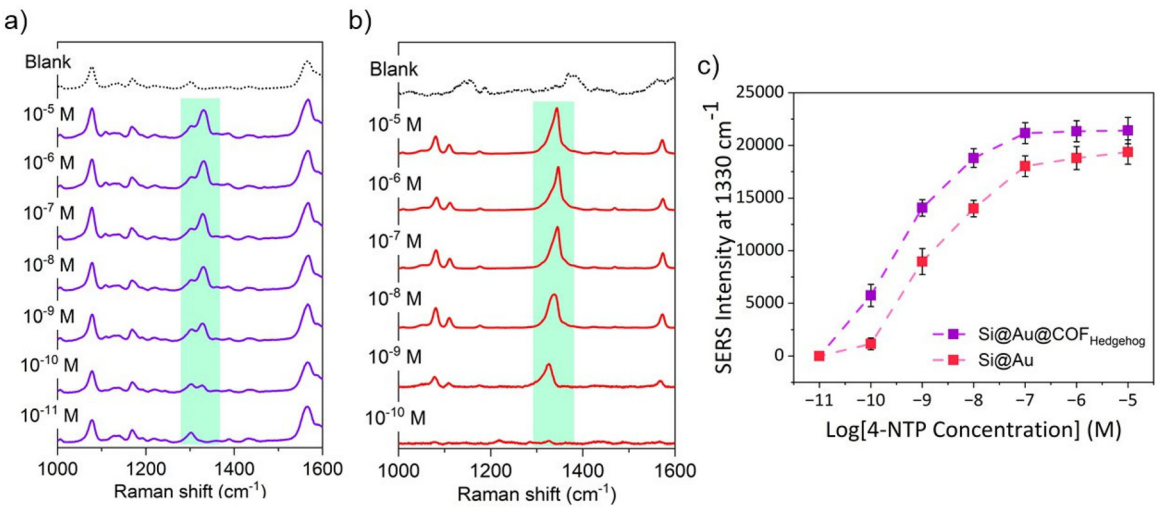

Fig. 5 SERS spectra of different concentrations of 4-NTP with (a) SiO_2@Au@$COF_{Hedgehog}$ and (b) SiO_2@Au plasmonic beads, respectively. The green area indicates the characteristic peak of 4-NTP centred at 1330 cm^{-1} (nitro group stretching). (c) Comparison of absolute SERS intensities of the 1330 cm^{-1} band for 4-NTP molecules with SiO_2@Au and SiO_2@Au@$COF_{Hedgehog}$. The dashed lines are guide to the eye.

This relatively fast interaction compared to plasmonic materials coated with other novel porous materials, such as MOFs,[8,66,67] can be attributed to the relatively large pore openings of the TAPB-DMTP COF of *ca.* 3 nm as compared to the size of 4-NTP (4.3 × 7.19 × 1.09 Å) (Fig. S18), enabling 4-NTP to access the plasmonic surface rapidly without clogging the pores of the COF shell even at the highest concentrations. Additionally, the shell thickness and morphology may allow for effective interactions with numerous 4-NTP probes in the environment. Moreover, due to the superior colloidal stability of the composite substrate and its ability to maintain this property in water for an extended period, SiO_2@Au@$COF_{Hedgehog}$ demonstrated higher SERS performance than the SiO_2@Au substrates.

Numerical simulations were carried out to shed light on the electromagnetic response of SiO_2@Au@$COF_{Hedgehog}$ (see the SI for details on the methodology). To this end, a single hybrid superstructure was modelled to characterize the capabilities of the material as SERS platform (Fig. 6a), focusing on the quantification of the enhancement of the electric field, or field enhancement (FE) (see the SI for the mathematical definition), around the metal, which in turn drives the enhanced Raman signal. The SiO_2 beads are an excellent substrate to provide colloidal stability to the Au NPs,[68] but they also become, together with the covering COF layer, a strong scatterer that contributes to the overall extinction of the system. This is evident from the simulated spectra in Fig. S19a, which shows a separation of the absorption due to the Au NPs and scattering cross-sections of the hybrid, the latter including the oscillating signature of higher order multipolar modes at short wavelengths.

These can also be found in the volume-averaged FE spectrum in Fig. 6a, driving a variation to the excitation of the metal NPs at high energies. At longer wavelengths, the plasmonic resonance of the Au NPs embedded in the COF is slightly red-shifted and noticeably broadened as compared to a single Au NP in a homogeneous medium with a comparable dielectric constant (Fig. S19b) due to their location at the interface between SiO_2 and the COF, as well as the appearance of interparticle interactions. Importantly, Au NP interparticle interactions are crucial for the measured SERS signal, as they provide strong electromagnetic hotspots that dominate in terms of their contribution to the signal due to the fourth power dependence of SERS on electric field amplitude,[69] thus quadratic on FE. The local FE maps in Fig. 6b show the spatial inhomogeneity of the enhancement for a composite system being illuminated at a laser wavelength of 785 nm. Notably, although a strong excitement of the main plasmonic mode of the Au NPs in the hybrid, *i.e.*, the single-particle mode, is not expected at this wavelength, resulting in an overall low expected average FE (Fig. 6a), a multiplicity of spots within the COF will present very strong enhancements due to NP–NP coupling (see Fig. 6c for a detailed view of Au dimer on the

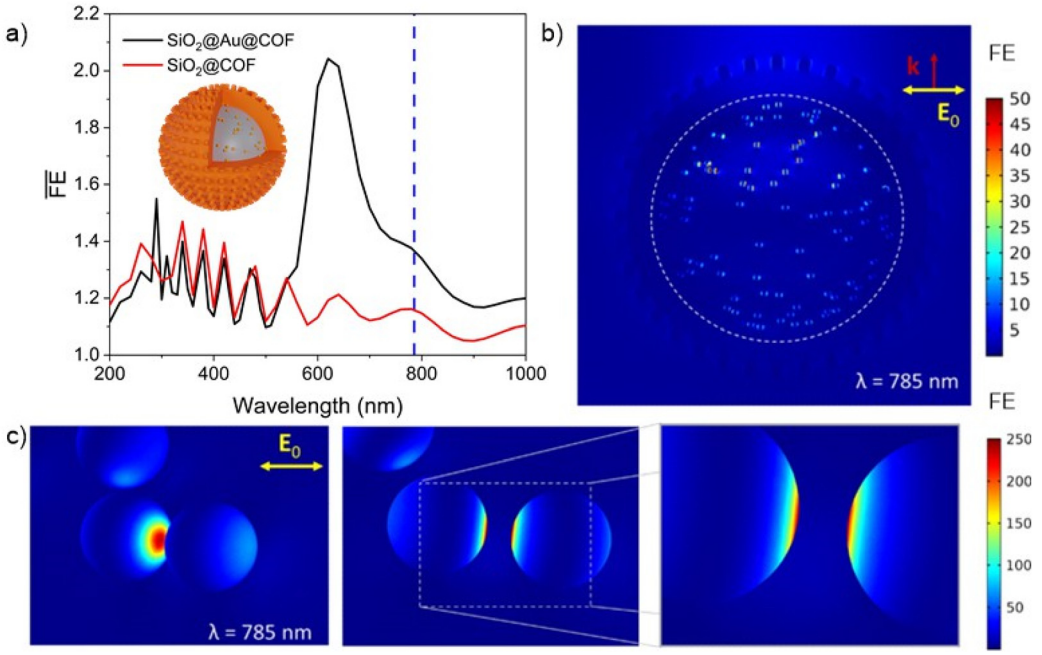

Fig. 6 (a) Volume-averaged field enhancement spectrum for SiO_2@Au@COF (black line) and the SiO_2@COF (red line) systems. The blue vertical dashed line indicates the experimental SERS excitation wavelength (785 nm). (b) Field enhancement map for SiO_2@Au@$COF_{Hedgehog}$ under 785 nm planewave with propagation direction and polarization as indicated. The white dashed circle indicates the outer boundary of the shell employed for the volume-averaged calculation, its inner boundary being the SiO_2 surface. The scale bar uses a reduced data range to showcase features other than the strongest hotspots. (c) Field enhancement maps for a hotspot between close Au NPs, marking the maximum FE in the system. Stronger hotspots are obtained when an Au NP dimer is closely aligned with the polarization of the incident wave and the pair is on a high-FE area in the SiO_2 scattering pattern (Fig. S19).

SiO_2 bead's surface). Such hotspots between NPs excited at 785 nm together with the increased local concentration of 4-NTP on the surface of the Au NPs due to the porosity of $COF_{Hedgehog}$ are responsible for the measured SERS signals. Insisting on the unequal contribution of different Au NPs to the SERS signal, it is also interesting to note that the particular pattern of the Mie scattering mode created by the SiO_2 bead introduces an additional spatial selection rule, so to speak, for the excited Au NPs. A demonstration of this can be seen in Fig. S19c and d, contrasting the FE map of the hybrid with that of a SiO_2@COF system without Au NPs, clearly showcasing the preferential excitation of the metal NPs according to the field pattern arising from the interaction of a linearly polarized planewave and the dielectrics.

After confirming the SERS performance of SiO_2@Au@$COF_{Hedgehog}$ with the probe molecule 4-NTP, the efficiency of the substrate was tested with a real-world target analyte. The herbicide terbutryn was chosen as the target as it is one of the priority substances with established environmental quality standard (EQS) at the EU level for water[70] due to its toxicity to numerous organisms in the ecosystem.[71–73] Terbutryn is usually analyzed in the laboratory using liquid or gas chromatography coupled to mass spectrometry (LC/GC-MS). New methods have been developed in the last years, such as liquid chromatography–quadrupole–time of flight–tandem mass spectrometry (LC-Q-ToF-MS/MS),[74] laser-induced forward transfer (LIFT),[75] photosynthesis inhibition-effect based analysis,[76] and chromatography coupled to UV-vis or mass spectrometry.[77] However, these methods are both time-consuming and challenging for low-level detection.

Before starting the SERS analysis of terbutryn with SiO_2@Au@$COF_{Hedgehog}$, an adsorption study was performed to understand if TAPB-DMTP COF is an appropriate "pre-concentrator" agent for terbutryn. Adsorption efficiency for terbutryn was determined by spiking ultrapure water with a concentration of 150 μg L^{-1}. After adsorption (19 °C, 45 min), COF_{Bulk} and $COF_{Hedgehog}$ particles were separated by centrifugation. Subsequently, analyte desorption using ethanol was performed, and the resulting sample was analyzed by HPLC-DAD. Under these conditions, both configurations of this COF adsorbed and preconcentrated terbutryn, showing 63 ± 4% for COF_{Bulk} and 53 ± 10% for $COF_{Hedgehog}$ of terbutryn adsorbed.

After demonstrating that $COF_{Hedgehog}$ efficiently adsorbs terbutryn, direct SERS detection was tested. Unfortunately, no variation was observed in the SERS fingerprint of SiO_2@Au@$COF_{Hedgehog}$ composite in the presence of terbutryn (Fig. S21a). We hypothesize that terbutryn molecules do not reach the gold surface because terbutryn is significantly larger (7.62 × 11.6 × 3.81 Å, Fig. S20) than 4-NTP (Fig. S18), and does not feature thiol moieties for enhanced affinity to the surface of plasmonic NPs. Although terbutryn is larger than 4-NTP, its molecular size is smaller than the COF pore (diameter of ~3 nm, Fig. S3). Therefore, terbutryn molecules may remain physically adsorbed on the pore surface or diffuse a few nanometers into the pores of the COF shell. To better understand where this herbicide is in the COF shell, a new composite with AuNPs decorated on the surface of the $COF_{Hedgehog}$ particles was prepared (COF@Au; Fig. S21b), and direct SERS detection was performed. Fig. S21b shows that the SERS fingerprint of the COF@Au composite displays variation with respect to the Raman spectra of $COF_{Hedgehog}$ particles. These differences could be due to variation in the deprotonated and protonated aldehyde and amine groups after gold growth. Also, this could be an effect of the plasmonic particles on the COF's vibrational modes. However, no evident variations were observed in the presence of terbutryn (Fig. S21b, orange spectrum). This supports the hypothesis that the molecules enter the pores and are not available to interact with AuNPs on the COF surface. These last results indicate that further optimization of the thickness of the COF shell must be performed to create a SiO_2@Au@$COF_{Hedgehog}$ composite applicable for direct SERS detection. We postulate that terbutryn exhibits stronger supramolecular interactions with the COF pores than with the AuNP surface. Nevertheless, a COF shell thinner than 15 nm may facilitate preconcentration of terbutryn in proximity to the gold surface, thereby enabling a measurable SERS response.

Consequently, an indirect SERS detection methodology was employed for the analytical detection of terbutryn (Fig. 7a). In the presence of terbutryn and upon exposure to 785 nm laser irradiation, 4-NTP was envisioned to undergo reduction to 4-ATP,[78] followed by dimerization to 4,4-dimercaptoazobenzene (DMAB) through plasmonic catalysis.[14,79] Although terbutryn acting as a reducing agent has not been reported, it can be oxidized and degraded slowly in water, with hydroxy-terbutryn as the major degradation product.[80] Therefore, terbutryn has redox properties that may trigger plasmon-induced redox reaction of 4-NTP to DMAB. First, equal amounts of SiO_2@Au@$COF_{Hedgehog}$ were treated with 4-NTP for 1 h ([4-NTP] = 10^{-8} M). Subsequently, the composite was collected by centrifugation and the pellet dispersed in water. Then, the samples were spiked with terbutryn at different concentrations ($[terbutryn]_{final}$ = 10^{-6}–10^{-10} M). After 1 h of incubation, the composites were collected by centrifugation and redispersed in water, and subsequently, SERS analysis was performed (785 nm laser, power 7.77 mW, and acquisition time 10 s) in liquid.

In the absence of terbutryn, the 4-NTP-functionalized composites exhibited the typical SERS fingerprint of the probe (4-NTP = 1330 cm^{-1}, 4-ATP = 1075 cm^{-1}, COF shell = 1564 cm^{-1}; Fig. 7b, blank). As 4-ATP is involved in COF anchoring, it is not expected to react through plasmonic catalysis. On the other hand, no intensity changes were found in the C=N stretching peak of the COF shell, rendering the ratiometric intensities of I_{1139}/I_{1564} and I_{1330}/I_{1564} as an acceptable internal standard. When the composites are treated with terbutryn (Fig. 7b, 10^{-6} M) and plasmonic catalysis takes effect, the intensity of the nitro peak at 1330 cm^{-1} significantly decreases, and three new peaks (1139, 1388, and 1431 cm^{-1}) emerge with high intensities. This suggests that terbutryn successfully reduces 4-NTP to 4-ATP, and under the influence of plasmonic catalysis, 4-ATP dimerizes to form DMAB (Fig. 7a and S22). Furthermore, as terbutryn concentration decreases, a

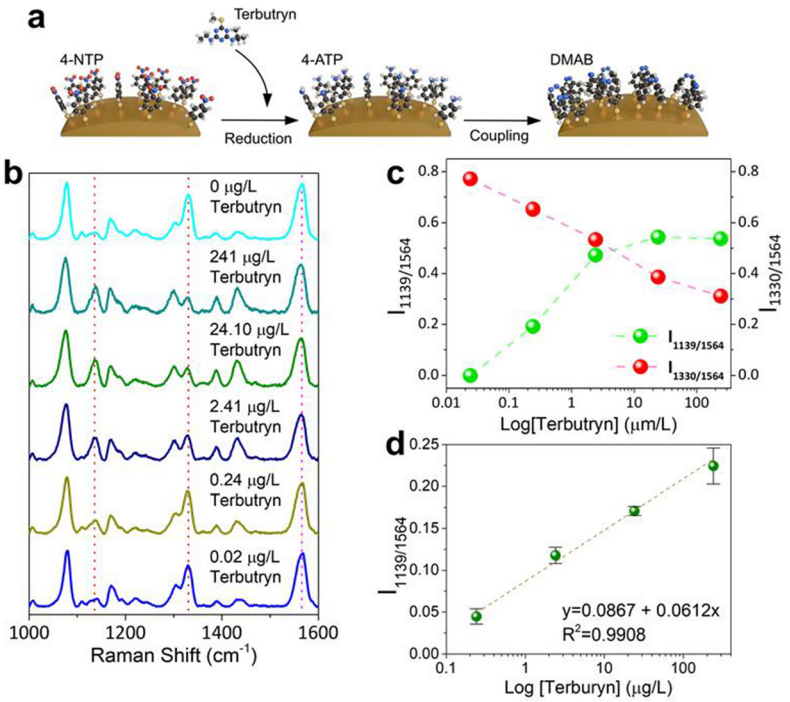

Fig. 7 (a) Schematic representation of the detection mechanism of terbutryn. Terbutryn triggers the plasmon-induced redox reaction of 4-NTP, reducing it to 4-ATP and forming the DMAB by dimerization. (b) SERS spectra of 4-NTP-functionalized SiO_2@Au@$COF_{Hedgehog}$ composites with different concentrations of terbutryn. (c) Comparison of ratiometric peak intensities of I_{1139}/I_{1564} and I_{1330}/I_{1564} *versus* the logarithmic molar concentration of terbutryn. (d) Calibration curve built by plotting I_{1139}/I_{1564} ratio against log [Terbutryn]. The LoD was calculated using equation $3.3\sigma/S$, where S is the slope of the calibration curve, and σ is the standard deviation of the response. Two independent replicates of the terbutryn detection, with three SERS spectra per replicate, were used to construct the calibration curve.

decrease in the intensity of the newly emerged DMAB peaks, as well as an increase in the dominant 4-NTP peak at 1330 cm^{-1}, are observed. Considering the COF shell peak as internal standard and normalizing the obtained results according to this peak, the ratiometric intensities of I_{1139}/I_{1564} and I_{1330}/I_{1564} are plotted in Fig. 7c as a function of terbutryn concentration. Accordingly, a calibration curve was constructed by plotting I_{1139}/I_{1564} against terbutryn concentration, obtaining a LoD for terbutryn of 10^{-9} M (220 ng L^{-1}) (Fig. 7d). We selected this ratio since both peaks are free of overlapping with other peaks presented in the SERS fingerprint (see Fig. 7b). Notably, this LoD is significantly lower than the one obtained with methods without pre-concentration, and those achieved by conventional methods such as LC-Q-ToF-MS/MS (10 μg L^{-1}),[81] LC-MS/MS (coupled with SPE 5 μg L^{-1}),[82] GC/IT (scan mode) (15 μg L^{-1}), or GC-MS/MS (26 μg L^{-1}),[83] and below the maximum accepted concentration in inland and other surface waters (340 ng L^{-1}) according to the EU EQS,[70] making the SiO_2@Au@$COF_{Hedgehog}$ composite a highly sensitive and efficient platform for environmental monitoring and analytical applications. We attribute this to the capacity of SiO_2@Au@$COF_{Hedgehog}$ to interact with a significant amount of terbutryn molecules due to its porous anisotropic shell and high colloidal stability. To test this, SiO_2@Au plasmonic beads without a COF shell were functionalized, similarly to the COF composite, with 10^{-8} M 4-NTP, and used for terbutryn detection at the highest concentration (10^{-6} M = 241 μg L^{-1}). Fig. S23a shows that the presence of terbutryn produces a reduction of 4-NTP only when it is adsorbed efficiently by the COF shell, as demonstrated by the reduction of the intensity of the SERS peak centred at 1330 cm^{-1} (nitro group stretching), and the appearance of new peaks (at 1139, 1388, and 1431 cm^{-1}) due to the formation of DMAB in the purple spectrum. The red spectrum in Fig. S23a, which was acquired after terbutryn incubation with SiO_2@Au@4-NTP Beads, does not show any spectral variation in comparison with the 4-NTP spectrum in the absence of terbutryn (Fig. 7b). UV-vis spectroscopy confirms (Fig. S23b) that almost no adsorption of terbutryn was produced by SiO_2@Au beads (similar absorbance to the initial terbutryn), while the absorbance band of terbutryn dropped significantly in the supernatant recovered from SiO_2@Au@$COF_{Hedgehog}$, demonstrating the high adsorption capacity of the COF shell for terbutryn in water.

A second control experiment was carried out, in which the AuNP-decorated $COF_{Hedgehog}$ NPs were functionalized with 4-NTP and incubated with 241 μg L^{-1} of terbutryn. Fig. S23c shows that a slight variation was observed in the 4-NTP spectrum in the presence of terbutryn: a slight decrease in the peak intensity centred at 1330 cm^{-1} (nitro group stretching). However, the characteristic peaks of the formation of DMAB

were not observed (see orange dashed lines that indicate the position of the DMAB peaks in Fig. S23). This demonstrates the importance of the SERS substrate configuration: COF shell is a key factor in triggering the adsorption of terbutryn molecules and concentrating them sufficiently close to the Au surface to enhance molecular interactions between terbutryn and 4-NTP. Also, this finding supports our hypothesis that terbutryn molecules do not remain on the COF surface but rather diffuse through the pores, having a stronger interaction with the COF than with AuNPs, preventing the direct detection of terbutryn.

Tables S3 and S4 summarize the latest advances in the fabrication of SERS substrates using COFs, and the SERS strategies used for the detection of terbutryn and other triazines, respectively. Interestingly, Table S3 shows that most of the SERS substates were fabricated by growing plasmonic nanoparticles on COF materials. The core–shell configuration of our SiO_2@Au@$COF_{Hedgehog}$ is the first, to the best of our knowledge, to be reported to date. This configuration has several advantages, such as improved selectivity due to the specific molecular size that can approach the plasmonic surface, which reduces the interference of the largest molecular weight compounds in the SERS fingerprints. Focusing on Table S4, our material outperformed the direct SERS strategies reported in other works: our LoD of 0.22 μg L^{-1} *versus* LoDs of 2 μg L^{-1} to 1 mg L^{-1} reported in the literature.

Conclusions

In conclusion, we successfully synthesized hedgehog-shaped COF particles through a simple one-step room temperature process. Extensive characterization revealed the unique morphology of the $COF_{Hedgehog}$ particles, their highly crystalline nature, colloidal stability, and mesoporous properties, rendering them promising candidates for various applications, including SERS spectroscopy. Following their growth at various time intervals allowed to gain insight into the mechanism of the formation of this morphology. Thereafter, a plasmonic hedgehog-shaped SiO_2@Au@$COF_{Hedgehog}$ composite was prepared and its utility as a SERS substrate was demonstrated. The composite exhibited a significantly high SERS intensity for 4-NTP as a probe molecule and a strong affinity by the Au surface *via* formation of an Au–S bond with a LoD of 10^{-10} M. Furthermore, we successfully applied the composite for the indirect SERS-based detection of toxic herbicide terbutryn. The composites demonstrated an excellent performance for terbutryn, a molecule with no affinity to the Au surface. This was possible thanks to the high adsorption efficiency of $COF_{Hedgehog}$ for terbutryn, attributed to the porous anisotropic COF shell and superior dispersion stability of the composite. This allowed the pre-concentration of terbutryn molecules sufficiently close to the Au surface, enhancing the interaction between terbutryn and 4-NTP and triggering a redox reaction with the nitro group of 4-NTP and the formation of DMAB. The indirect SERS detection of terbutryn showed a strong correlation between the intensity ratios of specific peaks, achieving an impressive LoD of 220 ng L^{-1}. Overall, this study highlights the potential of plasmonic hedgehog-shaped COF composites as unique and effective materials for SERS-based detection and paves the way for further research in this emerging field. The combination of such anisotropic COF morphology with plasmonic materials offers exciting opportunities for the design of sensitive and selective sensors for various target molecules, contributing to advancements in environmental analysis, biomedicine, and other fields requiring ultra-sensitive analytical techniques.

Author contributions

For author contributions, see the SI.

Conflicts of interest

There are no conflicts to declare.

Data availability

The data supporting this article have been included as part of the supplementary information (SI). Supplementary information is available. See DOI: https://doi.org/10.1039/d5nr02476e.

Acknowledgements

The authors are grateful for financial support by the INL and D4RUNOFF (Grant Agreement No.: 101060638, financed by the Horizon Europe program). LMS acknowledges financial support through the Ramón y Cajal grant RYC2020-030414-I funded by MICIU/AEI/10.13039/501100011033 and by "ESF Investing in your future" and the Spanish Ministry of Science and Innovation MCIN/AEI/FEDER (10.13039/501100011033) through the Syrocco project PID2022-137591NA-I00 *via* Proyectos de Generación de Conocimiento 2022. LRL acknowledges funding from the Fundação para a Ciência e a Tecnologia (FCT) for the 3rd. Scientific Employment Stimulus Program (2020.04021.CEECIND/CP1603/CT0002). MACD acknowledges financial support from the Spanish Ministerio de Ciencia e Innovación under projects, TED2021-132101B-I00/AEI/10.13039/501100011033, PID2020-113704RB-I00/AEI/10.13039/501100011033, PID2023-147495OB-I00 AEI/10.13039/501100011033, Xunta de Galicia/FEDER (IN607A 2018/5 and Centro Singular de Investigación de Galicia, Acc. 2019–2022, ED431G 2019-06), and 101080889 HORIZON-EIC-2022-PATHFINDERCHALLENGES-01-06 and 101115149 HORIZON-HLTH-2022-DISEASE-06-TWO-STAGE. LVB acknowledges financial support by MICIU/AEI/10.13039/501100011033 through the Ramón y Cajal grant RYC2021-033818-I and project PID2020-118282RA-I00. JGM acknowledges financial

support by MCIN/AEI/10.13039/501100011033 through project FPU21/03137. The authors acknowledge the use of scientific and technical services from Centro de Apoio Científico e Tecnolóxico á Investigación (CACTI-Universidade de Vigo) and kindly thank Dr Miguel Spuch-Calvar for the 3D illustrations.

References

1 C. J. Vörösmarty, P. B. McIntyre, M. O. Gessner, D. Dudgeon, A. Prusevich, P. Green, S. Glidden, S. E. Bunn, C. A. Sullivan, C. R. Liermann and P. M. Davies, *Nature*, 2010, **467**, 555–561.
2 M. Farhan Hanafi and N. Sapawe, *Mater. Today Proc.*, 2020, **31**, 141–150.
3 S. Rojas and P. Horcajada, *Chem. Rev.*, 2020, **120**, 8378–8415.
4 J. Langer, D. J. de Aberasturi, J. Aizpurua, R. A. Alvarez-Puebla, B. Auguié, J. J. Baumberg, G. C. Bazan, S. E. J. Bell, A. Boisen, A. G. Brolo, J. Choo, D. Cialla-May, V. Deckert, L. Fabris, K. Faulds, F. Javier García de Abajo, R. Goodacre, D. Graham, A. J. Haes, C. L. Haynes, C. Huck, T. Itoh, M. Käll, J. Kneipp, N. A. Kotov, H. Kuang, E. C. Le Ru, H. K. Lee, J. F. Li, X. Y. Ling, S. A. Maier, T. Mayerhöfer, M. Moskovits, K. Murakoshi, J. M. Nam, S. Nie, Y. Ozaki, I. Pastoriza-Santos, J. Perez-Juste, J. Popp, A. Pucci, S. Reich, B. Ren, G. C. Schatz, T. Shegai, S. Schlücker, L. L. Tay, K. George Thomas, Z. Q. Tian, R. P. van Duyne, T. Vo-Dinh, Y. Wang, K. A. Willets, C. Xu, H. Xu, Y. Xu, Y. S. Yamamoto, B. Zhao and L. M. Liz-Marzán, *ACS Nano*, 2020, **14**, 28–117.
5 X. Liu, J. Guo, Y. Li, B. Wang, S. Yang, W. Chen, X. Wu, J. Guo and X. Ma, *J. Mater. Chem. B*, 2021, **9**, 8378–8388.
6 L. Ouyang, W. Ren, L. Zhu and J. Irudayaraj, *Rev. Anal. Chem.*, 2017, **36**, 20160027.
7 T. Zorlu, M. A. Correa-Duarte and R. A. Alvarez-Puebla, *J. Chem. Phys.*, 2023, **158**, 171001.
8 C. Carrillo-Carrión, R. Martínez, M. F. Navarro Poupard, B. Pelaz, E. Polo, A. Arenas-Vivo, A. Olgiati, P. Taboada, M. G. Soliman, Ú. Catalán, S. Fernández-Castillejo, R. Solà, W. J. Parak, P. Horcajada, R. A. Alvarez-Puebla and P. del Pino, *Angew. Chem., Int. Ed.*, 2019, **58**, 7078–7082.
9 I. Haidar, G. Lévi, L. Mouton, J. Aubard, J. Grand, S. Lau-Truong, D. R. Neuville, N. Félidj and L. Boubekeur-Lecaque, *Phys. Chem. Chem. Phys.*, 2016, **18**, 32272–32280.
10 C. H. Lai, G. A. Wang, T. K. Ling, T. J. Wang, P. K. Chiu, Y. F. Chou Chau, C. C. Huang and H. P. Chiang, *Sci. Rep.*, 2017, **7**, 5446.
11 A. Mariño-Lopez, A. Sousa-Castillo, M. Blanco-Formoso, L. N. Furini, L. Rodríguez-Lorenzo, N. Pazos-Perez, L. Guerrini, M. Pérez-Lorenzo, M. A. Correa-Duarte and R. A. Alvarez-Puebla, *ChemNanoMat*, 2019, **5**, 46–50.
12 C. Huang, A. Li, X. Chen and T. Wang, *Small*, 2020, **16**, 2004802.
13 H. Qin, S. Zhao, H. Gong, Z. Yu, Q. Chen, P. Liang and D. Zhang, *Biosensors*, 2023, **13**, 479.
14 T. Zorlu, I. B. Becerril-Castro, B. Puertolas, V. Giannini, M. A. Correa-Duarte and R. A. Alvarez-Puebla, *Angew. Chem., Int. Ed.*, 2023, **62**, e202305299.
15 B. X. Wang, G. Duan, W. Xu, C. Xu, J. Jiang, Z. Yang, Y. Wu and F. Pi, *Crit. Rev. Food Sci. Nutr.*, 2024, **64**, 472–516.
16 H. C. Zhou, J. R. Long and O. M. Yaghi, *Chem. Rev.*, 2012, **112**, 673–674.
17 G. Zheng, I. Pastoriza-Santos, J. Pérez-Juste and L. M. Liz-Marzán, *SmartMat*, 2021, **2**, 446–465.
18 W. Li, X. Xia and S. Li, *ACS Appl. Mater. Interfaces*, 2020, **12**, 3265–3273.
19 Y. Wei, F. Zhang, J. Hao, Y. Ling, Y. Gong, S. Wang, J. Wei and Z. Yang, *Appl. Catal., B*, 2020, **272**, 119035.
20 Y. Song, J. Phipps, C. Zhu and S. Ma, *Angew. Chem., Int. Ed.*, 2023, **62**, e202216724.
21 Z. Xia, Y. Zhao and S. B. Darling, *Adv. Mater. Interfaces*, 2021, **8**, 2001507.
22 S. P. S. Fernandes, V. Romero, B. Espiña and L. M. Salonen, *Chem. – Eur. J.*, 2019, **25**, 6461–6473.
23 Y. Liu, K. K. Chui, Y. Fang, S. Wen, X. Zhuo and J. Wang, *ACS Nano*, 2024, **18**, 11234–11244.
24 N. Yang, H. Pu and D. W. Sun, *Food Chem.*, 2024, **446**, 138846.
25 A. M. Evans, M. R. Ryder, W. Ji, M. J. Strauss, A. R. Corcos, E. Vitaku, N. C. Flanders, R. P. Bisbey and W. R. Dichtel, *Faraday Discuss.*, 2021, **225**, 226–240.
26 Q. Wei, L. Shao, H. Pu and D. W. Sun, *J. Food Meas. Charact.*, 2024, **18**, 2903–2915.
27 R. Tan, M. Zeng, Q. Huang, N. Zhou, M. Deng, Y. Li and X. Luo, *Food Chem.*, 2024, **457**, 140166.
28 W. F. Huang, H. B. Xu, S. C. Zhu, Y. He, H. Y. Chen and D. W. Li, *ACS Sens.*, 2024, **9**, 2421–2428.
29 S. Kandambeth, V. Venkatesh, D. B. Shinde, S. Kumari, A. Halder, S. Verma and R. Banerjee, *Nat. Commun.*, 2015, **6**, 6786.
30 B. J. Smith, L. R. Parent, A. C. Overholts, P. A. Beaucage, R. P. Bisbey, A. D. Chavez, N. Hwang, C. Park, A. M. Evans, N. C. Gianneschi and W. R. Dichtel, *ACS Cent. Sci.*, 2017, **3**, 58–65.
31 R. L. Li, N. C. Flanders, A. M. Evans, W. Ji, I. Castano, L. X. Chen, N. C. Gianneschi and W. R. Dichtel, *Chem. Sci.*, 2019, **10**, 3796–3801.
32 Y. Zhao, L. Guo, F. Gándara, Y. Ma, Z. Liu, C. Zhu, H. Lyu, C. A. Trickett, E. A. Kapustin, O. Terasaki and O. M. Yaghi, *J. Am. Chem. Soc.*, 2017, **139**, 13166–13172.
33 J. H. Bahng, B. Yeom, Y. Wang, S. O. Tung, J. D. Hoff and N. Kotov, *Nature*, 2015, **517**, 596–599.
34 D. G. Montjoy, J. H. Bahng, A. Eskafi, H. Hou and N. A. Kotov, *J. Am. Chem. Soc.*, 2018, **140**, 7835–7845.
35 G. Das, T. Skorjanc, T. Prakasam, B. Garai, S. Abubakar, C. S. Zalch, F. Gándara, R. Pasricha, S. K. Sharma, S. Varghese, R. Jagannathan, M. A. Olson and A. Trabolsi, *ACS Appl. Nano Mater.*, 2022, **5**, 13745–13751.
36 S. Kim, C. Park, M. Lee, I. Song, J. Kim, M. Lee, J. Jung, Y. Kim, H. Lim and H. C. Choi, *Adv. Funct. Mater.*, 2017, **27**, 1700925.

37 Q. L. Wen, W. Z. She, J. Z. Liu, H. C. Zhang, R. S. Li, J. Ling and Q. Cao, *Microporous Mesoporous Mater.*, 2023, **357**, 112624.
38 Y. Deng, Y. Wang, J. Wang, Z. Wei, C. Xin, J. Liu, C. Zhao and Z. Zhang, *Mater. Today Chem.*, 2022, **26**, 101027.
39 L. Chen, W. Wang, J. Tian, F. Bu, T. Zhao, M. Liu, R. Lin, F. Zhang, M. Lee, D. Zhao and X. Li, *Nat. Commun.*, 2021, **12**, 4556.
40 H. Xu, J. Gao and D. Jiang, *Nat. Chem.*, 2015, **7**, 905–912.
41 T. Zhang, C. Gao, W. Huang, Y. Chen, Y. Wang and J. Wang, *Talanta*, 2018, **188**, 578–583.
42 H. Chu, X. Sun, X. Zha, Y. Zhang and Y. Wang, *Colloids Surf., A*, 2022, **648**, 129238.
43 Q. Fang, Z. Pang, Q. Ai, Y. Liu, T. Zhai, D. Steinbach, G. Gao, Y. Zhu, T. Li and J. Lou, *Proc. Natl. Acad. Sci. U. S. A.*, 2023, **120**, e2208676120.
44 J. M. Rotter, S. Weinberger, J. Kampmann, T. Sick, M. Shalom, T. Bein and D. D. Medina, *Chem. Mater.*, 2019, **31**, 10008–10016.
45 M. Traxler and W. R. Dichtel, *Chem. Sci.*, 2024, **15**, 7545–7551.
46 W. Ma, Q. Zheng, Y. He, G. Li, W. Guo, Z. Lin and L. Zhang, *J. Am. Chem. Soc.*, 2019, **141**, 18271–18277.
47 C. G. Gruber, L. Frey, R. Guntermann, D. D. Medina and E. Cortés, *Nature*, 2024, **630**, 872–877.
48 L. Deng, W. Chen, G. Zhou, Y. Liu, L. Liu, Y. Han, Z. Huang and D. Jiang, *J. Am. Chem. Soc.*, 2024, **146**, 35427–35437.
49 J. Li, Y. Liu, X. Tian, S. Chen, S. Tao, M. Takeguchi and D. Jiang, *J. Am. Chem. Soc.*, 2025, **147**, 26955–26968.
50 A. M. Elewa, A. F. M. El-Mahdy, A. E. Hassan, Z. Wen, J. Jayakumar, T. L. Lee, L. Y. Ting, I. M. A. Mekhemer, T. F. Huang, M. H. Elsayed, C. L. Chang, W. C. Lin and H. H. Chou, *J. Mater. Chem. A*, 2022, **10**, 12378–12390.
51 A. R. Bagheri and N. Aramesh, *J. Mater. Sci.*, 2021, **56**, 1116–1132.
52 W. Ma, Q. Zheng, Y. He, G. Li, W. Guo, Z. Lin and L. Zhang, *J. Am. Chem. Soc.*, 2019, **141**, 18271–18277.
53 B. J. Smith, A. C. Overholts, N. Hwang and W. R. Dichtel, *Chem. Commun.*, 2016, **52**, 3690–3693.
54 Q. Lu, X. Zhao, Y. Jiang, K. Zhao and J. Pan, *Chem. Eng. J.*, 2024, **499**, 156308.
55 T. Zorlu, B. Puértolas, I. B. Becerril-Castro, L. Guerrini, V. Giannini, M. A. Correa-Duarte and R. A. Alvarez-Puebla, *ACS Nanosci. Au*, 2023, **3**, 222–229.
56 D. Lupa, M. Oćwieja, N. Piergies, A. Baliś, C. Paluszkiewicz and Z. Adamczyk, *Colloid Interface Sci. Commun.*, 2019, **33**, 100219.
57 Y. Li, C. X. Yang and X. P. Yan, *Chem. Commun.*, 2017, **53**, 2511–2514.
58 V. Romero, S. P. S. Fernandes, L. Rodriguez-Lorenzo, Yu. V. Kolen'ko, B. Espiña and L. M. Salonen, *Nanoscale*, 2019, **11**, 6072–6079.
59 V. Romero, S. P. S. Fernandes, L. P. L. Gonçalves, O. Oliveira, M. Meledina, K. Strutyński, M. Melle-Franco, Yu. V. Kolen'ko, B. Espiña and L. M. Salonen, *CrystEngComm*, 2023, **25**, 2456–2462.
60 Y. Yang, Z. Su, D. Wu, J. Liu, X. Zhang, Y. Wu and G. Li, *Anal. Chim. Acta*, 2022, **1218**, 340000.
61 W. Wang, W. Wang, L. Liu, L. Xu, H. Kuang, J. Zhu and C. Xu, *ACS Appl. Mater. Interfaces*, 2016, **8**, 15591–15597.
62 S. Chen, J. Fan, M. Lv, C. Hua, G. Liang and S. Zhang, *Anal. Chem.*, 2022, **94**, 14675–14681.
63 P. Innocenzi and L. Malfatti, *TrAC, Trends Anal. Chem.*, 2019, **114**, 233–241.
64 M. Lv, X. Wu, W. Wang, D. Han, S. Chen, Y. Hu, Q. Zhang, Q. Wang and R. Wei, *ACS Sens.*, 2025, **10**, 1778–1787.
65 L. M. Quynh, N. H. Nam, K. Kong, N. T. Nhung, I. Notingher, M. Henini and N. H. Luong, *J. Electron. Mater.*, 2016, **45**, 2563–2568.
66 G. Zheng, S. de Marchi, V. López-Puente, K. Sentosun, L. Polavarapu, I. Pérez-Juste, E. H. Hill, S. Bals, L. M. Liz-Marzán, I. Pastoriza-Santos and J. Pérez-Juste, *Small*, 2016, **12**, 3935–3943.
67 G. Gumilar, J. Henzie, B. Yuliarto, A. Patah, N. Nugraha, M. Iqbal, M. A. Amin, M. S. A. Hossain, Y. Yamauchi and Y. V. Kaneti, *J. Mater. Chem. A*, 2022, **10**, 6662–6678.
68 Y. Negrín-Montecelo, A. H. A. Geneidy, A. O. Govorov, R. A. Alvarez-Puebla, L. V. Besteiro and M. A. Correa-Duarte, *ACS Photonics*, 2023, **10**, 3310–3320.
69 P. L. Stiles, J. A. Dieringer, N. C. Shah and R. P. Van Duyne, *Annu. Rev. Anal. Chem.*, 2008, **1**, 601–626.
70 U. Förstner, *J. Soils Sediments*, 2009, **9**, 89–93.
71 N. Min, H. Park, T. Hong, J. Song, G. Song and W. Lim, *Sci. Total Environ.*, 2023, **893**, 164839.
72 D. Fernández-Calviño, J. Rousk, E. Bååth, U. E. Bollmann, K. Bester and K. K. Brandt, *Soil Biol. Biochem.*, 2021, **154**, 108130.
73 Q. Xing, Y. W. Kim, J. S. Park, Y. S. Han, C. Yarish, H. I. Yoo and J. K. Kim, *J. Appl. Phycol.*, 2023, **35**, 1663–1671.
74 R. Brix, N. Bahi, M. J. L. De Alda, M. Farré, J. M. Fernandez and D. Barceló, *J. Mass Spectrom.*, 2009, **44**, 330–337.
75 M. Chatzipetrou, F. Milano, L. Giotta, D. Chirizzi, M. Trotta, M. Massaouti, M. R. Guascito and I. Zergioti, *Electrochem. Commun.*, 2016, **64**, 46–50.
76 P. Booij, A. D. Vethaak, P. E. G. Leonards, S. B. Sjollema, J. Kool, P. De Voogt and M. H. Lamoree, *Environ. Sci. Technol.*, 2014, **48**, 8003–8011.
77 H. W. Jang, J. Lee, H. Choi, T. G. Nam, S. H. Kim and K. G. Lee, *Food Sci. Biotechnol.*, 2018, **27**, 1525–1530.
78 L. A. Montoya and M. D. Pluth, *Chem. Commun.*, 2012, **48**, 4767–4769.
79 W. Xie, B. Walkenfort and S. Schlücker, *J. Am. Chem. Soc.*, 2013, **135**, 1657–1660.
80 T. Junginger, S. Payraudeau and G. Imfeld, *Chemosphere*, 2022, **305**, 135329.
81 Z. Tang, Y. Wei, D. Wang, J. Huang, N. Wan, J. Wei and B. Li, *J. Food Compos. Anal.*, 2023, **123**, 105638.
82 L. Ramadan, I. Ozturk-Ufuk, E. Yuksel and E. Topuz, *Water, Air, Soil Pollut.*, 2024, **235**, 537.
83 H. W. Jang, J. Lee, H. Choi, T. G. Nam, S. H. Kim and K. G. Lee, *Food Sci. Biotechnol.*, 2018, **27**, 1525–1530.